

Simulating Sinking Satellites with SUPERBOX-10

R. Bien^{*}, T. Brandt, A. Just[†]

Astronomisches Rechen-Institut, Zentrum für Astronomie, University of Heidelberg, Mönchhofstr. 12-14, 69120 Heidelberg, Germany

Accepted 2012 October 3. Received 2012 July 27; in original form 2012 January 23

ABSTRACT

SUPERBOX-10 is the successor of SUPERBOX, a particle-mesh code where additional grids and sub-grids are applied to regions of high particle density. Previous limitations have been solved. For instance, the vertical resolution is improved considerably when flattened grids are used. Since the computationally most intensive part is the Fast Fourier Transform, we introduce a parallelised version using the library FFTW, resulting in a speed-up of a few. The new features are tested using a galaxy model consisting of an exponential disc, a bulge and a dark matter halo. We demonstrate that the use of flattened grids efficiently reduces numerical heating. We simulate the merging of disc-bulge-halo galaxies with small spherical satellites. As a result, satellites on orbits with both low eccentricity and inclination heat the disc most efficiently. Moreover, we find that most of the satellite’s energy and angular momentum is transferred to the halo.

Key words: methods: numerical – stellar dynamics – galaxies: evolution – galaxies: kinematics and dynamics – galaxies: structure.

1 INTRODUCTION

Observations of stars in the solar neighbourhood show an increase of the velocity dispersion (the random motion) proportional to $t^{0.3\dots0.6}$, where t is the stellar age (Wielen 1977; Holmberg, Nordström & Andersen 2007). This effect can be interpreted as a heating of the Galactic disc with time. However, it is unclear what is the cause of this heating. Several mechanisms have been proposed: Massive black holes in the galactic halo as a source of heating were investigated by Lacey & Ostriker (1985), Wielen & Fuchs (1990), Rix & Lake (1999) and Hänninen & Flynn (2002), but seem to be excluded by observations. Ardi, Tsuchiya & Burkert (2003) considered massive clumps of dark matter as a possible heating agent. Giant molecular clouds were found to cause mostly vertical heating by Lacey (1984) and later Hänninen & Flynn (2002). Carlberg & Sellwood (1985) and Carlberg (1987) show that transient spiral waves heat efficiently in the Galactic plane. Lastly, Quinn, Hernquist & Fullagar (1993) and Velazquez & White (1999) simulate merging with small satellites and find both radial and vertical heating. This last mechanism is discussed in this paper. It should be mentioned, however, that radial mixing may influence the age-velocity dispersion relation significantly (Schönrich & Binney 2009; Sellwood & Binney 2001; Roškar et al. 2008).

The merging of galaxies can be divided into three categories according to their mass ratios. Major mergers with mass ratios 1:1 to 1:3 of the total galaxy masses usually destroy discs and result in an early type remnant (Naab, Jesseit & Burkert 2006, and references therein). Minor mergers with mass ratios 1:3 to 1:10 of the total galaxy masses destroy a thin disc (Purcell, Bullock & Kazantzidis 2010). The minor merger events are discussed in the context of the formation of thick discs (Villalobos & Helmi 2008, 2009) and substructure in the halo (Newberg et al. 2002; Purcell, Bullock & Kazantzidis 2010). The third category is the merging of satellite galaxies (or dark matter clumps) with smaller mass ratios. These merger or interaction events can be characterized as a perturbation of the primary galaxy and it is more convenient to quantify the mass ratio in units of the disc mass of the primary. In this context the survival of a thin disc over 10 Gyr in a Λ CDM universe lead to serious constraints on the clumpiness of the DM halo (Ardi, Tsuchiya & Burkert 2003). Hopkins et al. (2008) compared the efficiency of the disc by satellite galaxy mergers of different authors and argued that it scales with the square of the satellite mass. This is consistent with the interpretation heating by dynamical friction during each disc crossing event. As a consequence, the upper mass end of the perturbers are most efficient and determine the survival of a thin disc. Kazantzidis et al. (2008, 2009) performed a comprehensive study of the impact of DM subhaloes on a Milky Way like disc galaxy in a realistic cosmological

^{*} E-mail: reinhold@ari.uni-heidelberg.de

[†] E-mail: just@ari.uni-heidelberg.de

context. They investigated the resulting substructures and kinematic features in disc and halo.

In numerical simulations the long-term (or secular) dynamical evolution of a thin galactic disc is very sensitive to the spatial resolution, the level of numerical noise, and the dynamical feedback with the DM halo. A live dark matter halo is important for two reasons. Velazquez & White (1999) have shown that the reaction of the disc on the perturbation of a satellite galaxy is significantly higher with a live halo compared to a rigid dark matter potential. Secondly, dynamical friction in the dark matter is important for the orbital evolution and thus energy loss of satellites with masses exceeding $\sim 10^8 M_{\odot}$. This is exactly the mass range dominating the heating rate of the disc by satellite galaxies. Additionally, the mass of the dark matter particle must not be too large in order to avoid numerical heating of the disc. In most simulations the disc is represented by less than 1 million particles leading to a significant thickening of the disc by numerical two-body relaxation, which is much stronger in direct N -body codes and Tree codes compared to particle mesh-codes. In Velazquez & White (1999) and in Hayashi & Chiba (2006) the numerical heating of the unperturbed disc was shown explicitly. Velazquez & White (1999) used a differential method to quantify the dynamical heating of infalling satellites. This may underestimate the heating rate, since a more realistic thinner, dynamically cooler, disc is more sensitive to perturbations. On the other hand, the feedback on the satellite galaxy may be larger by the stronger disc shocking event. Particle-mesh codes are predestined for the simulation of collisionless systems such as galaxies, because two-body relaxation is strongly suppressed by the partial decoupling of the point-like structure in orbital motion of the particles and the gravitational potential based on the grid. Khoperskov et al. (2007) have shown that the growth of global mode perturbations are easily damped out by noise due to an insufficient particle number. If the excitation of spiral structure or bar-like perturbations are an important mechanism for the energy transfer from the satellite to the disc, then a very high resolution well above 1 million particles is needed to reproduce a realistic heating rate.

Improving the resolution of discs in vertical direction has always been a challenge. There is, indeed, a further problem which is inherent in any numerical technique that is used for the simulation of disc galaxies. Stellar discs have relaxation times larger than a Hubble time, i. e. they are collisionless systems. This implies that in simulations the thickness of an unperturbed disc indicates how well the code would model a collisionless gravitating system. The term “unperturbed” denotes the absence of perturbations such as stellar bars, spiral arms, or molecular clouds. One often notes, in simulations, that discs become thicker with time. This is caused by the graininess of the particle distribution and the limited spatial resolution. We refer to this effect as “numerical heating”.

For two decades SUPERBOX is used as a successful tool to simulate the dynamics of isolated and interacting galaxies. A first description was given by Bien, Fuchs & Wielen (1991), together with a consideration of the direct N -body technique and a tree-code. For a more detailed discussion the reader is referred to Fellhauer et al. (2000). We also men-

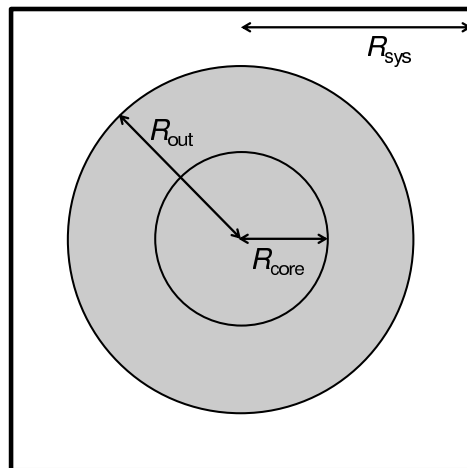


Figure 1. Projection of a simplified galaxy model in a 3D box. Shown are the basic parameters R_{core} , R_{out} and R_{sys} .

tion Fellhauer’s lecture notes (Fellhauer 2008). The code was evolving from the conventional particle-mesh technique (see, e. g., Hockney & Eastwood 1988) by applying grids and subgrids in regions of high particle density. The advantage of SUPERBOX is that the code can run on any workstation or PC, giving reliable results. The code thus proves to be a serious alternative to direct N -body schemes and tree-codes.

Initially, Madejsky & Bien (1993) applied SUPERBOX to compare numerical experiments to observations of the high-velocity encounter of NGC 4782/4783. They found a convincing description of the morphological and kinematical structure, and estimated the time elapsed since the closest approach of the two interacting galaxies. This was the beginning of a series of research projects using SUPERBOX as a tool. We note as examples the dynamical evolution of a satellite galaxy (Klessen & Kroupa 1998), the decay of dwarf galaxies in dark matter haloes (Peñarrubia, Kroupa & Boily 2002), and dynamical friction, compare Peñarrubia, Just & Kroupa (2004) and Just & Peñarrubia (2005). It should be mentioned that Spinnato et al. (2003) studied the inspiral of a black hole to the Galactic centre, and Khoperskov et al. (2007) considered unstable modes in a disc. Fellhauer et al. (2008) published on the dynamics of the Bootes dwarf galaxy. Peñarrubia, Navarro & McConnachie (2008) investigated the tidal evolution of dwarfs of the Local Group. Most recently, a study was made on the dynamical friction of massive objects in galactic centres by Just et al. (2011). Our list is by far not complete.

So far, SUPERBOX was not able to adapt the subgrids to discs. A higher resolution in vertical direction can be achieved by introducing flattened grids, see Bien et al. (2008). This new feature and the application to dynamical heating of galactic discs are the main topics of the present paper. The improved code is called SUPERBOX-10. As SUPERBOX, SUPERBOX-10 is rather free of numerical heating.

Below we first describe SUPERBOX in detail and then

extend to SUPERBOX-10. It follows a discussion of the parallelised version which results in a significant speed-up. Then our test of improved vertical resolution is described. As an important application we consider disc heating by satellite galaxies. In particular, we address the ratio of radial and vertical velocity dispersion and the transfer of energy and angular momentum. Special attention is given to the interaction of the infalling satellite with the dark matter halo.

In a conference proceedings publication (Bien et al. 2008) we presented preliminary results on an improved version of SUPERBOX with increased vertical resolution of the disc: Negligible disc thickening of an isolated disc after 2.5 Gyr. The present paper should be seen as a pilot study for high resolution simulations of disc heating by satellite galaxy mergers. Two new aspects are presented: (1) No correction for numerical heating is needed and we can measure the heating rate directly. Dynamical friction in the dark matter halo is included automatically. (2) We analyse for the first time additionally the transfer of angular momentum. This is important for understanding the physical processes responsible for the disc heating. For this pilot study we select a satellite with a relatively high mass on eccentric orbits, which is destroyed after a few disc crossing events.

2 A REVIEW OF SUPERBOX

2.1 Basic concepts

The conventional particle-mesh technique considers a set of massive particles, often called “superstars”, in a three-dimensional Cartesian grid (“box”) consisting of $N \times N \times N$ cells which represents a relevant part of the universe. In this section, the length of each cell is the unity. We suppose that $\rho_{a,b,c}$ is the mean density in the cell with indices a, b, c which are integers running from 0 to $N-1$. Then the potential can be obtained by solving Poisson’s equation

$$\Phi_{a,b,c} = G \sum_{\xi=0}^{N-1} \sum_{\eta=0}^{N-1} \sum_{\zeta=0}^{N-1} \rho_{\xi,\eta,\zeta} H_{\xi-a,\eta-b,\zeta-c} \quad (1)$$

Here, $H_{\xi-a,\eta-b,\zeta-c}$ (i. e. Green’s function) is the inverse distance between the points having indices a, b, c and ξ, η, ζ , namely

$$H_{\xi-a,\eta-b,\zeta-c} = [(\xi-a)^2 + (\eta-b)^2 + (\zeta-c)^2]^{-1/2} \quad (2)$$

We note that the term $G\rho_{\xi,\eta,\zeta}H_{\xi-a,\eta-b,\zeta-c}$ accounts for the contribution of the cell ξ, η, ζ to the cell a, b, c . Thus $\Phi_{a,b,c}$ gives the correct potential assigned to cell a, b, c . The evaluation of all $N \times N \times N$ values $\Phi_{a,b,c}$ takes a time proportional to the number of cells squared, $(N \times N \times N)^2$.

The direct convolution can be replaced by discrete Fourier transforms where N is supposed to be a power of 2. First $\rho_{a,b,c}$ and $H_{a,b,c}$ are transformed, resulting in

$$\hat{\rho}_{k,l,m} = \sum_{a=0}^{N-1} \sum_{b=0}^{N-1} \sum_{c=0}^{N-1} \rho_{a,b,c} \exp[-i\frac{2\pi}{N}(ka+lb+mc)] \quad (3)$$

and $\hat{H}_{k,l,m}$, analogously. The potential is then obtained by the inverse transformation of the product $\hat{\rho}_{k,l,m}\hat{H}_{k,l,m}$,

$$\Phi_{a,b,c} =$$

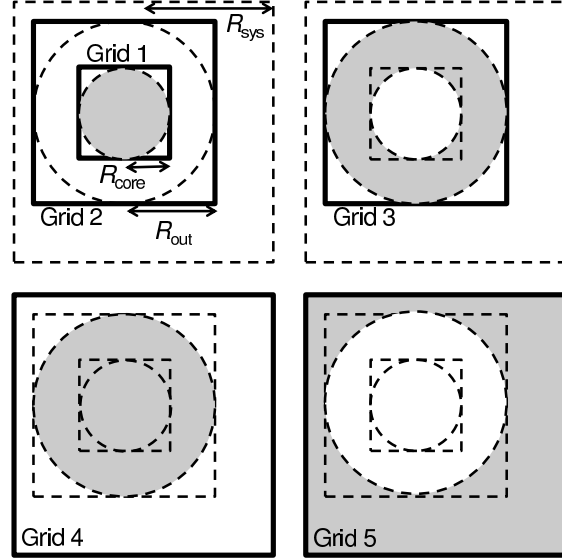


Figure 2. The five grids of SUPERBOX. Grid 1 has the highest resolution and resolves the core. Grid 1, grid 2 and grid 3 move through the local universe, defined by grid 4 and grid 5.

$$\frac{G}{N^3} \sum_{k=0}^{N-1} \sum_{l=0}^{N-1} \sum_{m=0}^{N-1} \hat{\rho}_{k,l,m} \hat{H}_{k,l,m} \exp[+i\frac{2\pi}{N}(ka+lb+mc)] \quad (4)$$

The procedure can dramatically be accelerated when a Fast Fourier Transform (FFT) is applied. The computing time is then roughly proportional to $N^3 \log N$.

The potential, as derived so far by Fourier transforms, is correct for periodic systems only. The exact potential of isolated systems can be obtained by doubling the number of cells in each coordinate direction, i. e. a grid is considered which contains $2N \times 2N \times 2N$ cells. A rigorous proof can be found in the paper by Eastwood & Brownrigg (1979). As before, the $N \times N \times N$ sub-grid contains the particles (“active region”). The remaining space is left empty. Likewise, H is extended over the $2N \times 2N \times 2N$ cells such that it satisfies

$$\begin{aligned} H_{2N-a,b,c} &= H_{2N-a,2N-b,c} \\ &= H_{2N-a,b,2N-c} = H_{2N-a,2N-b,2N-c} = H_{a,2N-b,c} \\ &= H_{a,2N-b,2N-c} = H_{a,b,2N-c} = H_{a,b,c} \end{aligned} \quad (5)$$

for $0 \leq a, b, c \leq N$. Having transformed the extended functions ρ and H , the correct potential Φ can be found in the active grid. Outside, Φ is unphysical.

Numerical differentiation of the potential with respect to the coordinates leads for each particle j to the acceleration $(a_x)_j, (a_y)_j, (a_z)_j$. The leap-frog scheme is applied to integrate the equations of motions. In x -direction the algorithm reads

$$\begin{aligned} \dot{x}_j(t + \Delta t/2) &= \dot{x}_j(t - \Delta t/2) + \Delta t(a_x)_j \\ x_j(t + \Delta t) &= x_j(t) + \Delta t\dot{x}_j(t + \Delta t/2) \end{aligned} \quad (6)$$

where t is the time and Δt denotes the constant integration step.

The particle-mesh technique holds some subtle twists. For instance for $H_{a,b,c}$ it suffices a $(N+1) \times (N+1) \times (N+1)$

grid. From the symmetry conditions (5) follows that the function is then known on the whole $2N \times 2N \times 2N$ grid. The sub-grid is overwritten by \hat{H} which shows similar symmetries. \hat{H} is calculated only once, since it is fixed over the integration period. For each integration step the grid containing the density ρ is overwritten by the Fourier transform ($\hat{\rho}$ which, in turn, is overwritten by $\hat{\rho}\hat{H}$). This product is finally overwritten by Φ . The advantages of the method are obvious. The conventional particle-mesh technique was orders of magnitude faster than direct N -body codes at the time. This allows the integration of a large number of particles. Thus, statistical noise is extremely low. Particles leaving the outermost grid are lost. The user should thus carefully consider the number of particles involved in the computation.

The greatest disadvantage, however, is the low spatial resolution in regions of higher particle densities, e.g. the cores of spherical galaxies. An improvement is SUPERBOX which treats the particles self-consistently in a nested system of grids. Here, the term “self-consistent” means that all particles have masses which define the total potential. For simplicity, we consider a spherical galaxy of radius R_{out} . Fig. 1 shows how the particles are subdivided into a central region (“core”) where the distance r from the centre is $< R_{\text{core}}$ and a region with $R_{\text{core}} < r < R_{\text{out}}$. The local universe is given by R_{sys} .

As shown in Fig. 2 SUPERBOX utilises five grids. They all have the same number of cells, N^3 .

- (i) Grid 1 has the highest resolution and resolves the core which contains all particles with $< R_{\text{core}}$.
- (ii) Grid 2 contains the core, too, but the resolution is intermediate.
- (iii) Grid 3 is equal to grid 2, but contains only particles with $R_{\text{core}} < r < R_{\text{out}}$.
- (iv) Grid 4 is the fixed global grid. It contains only particles inside R_{out} .
- (v) Grid 5 is equal to grid 4 with all particles outside R_{out} .

As the galaxy moves, grid 1, grid 2 and grid 3 move through the local universe (i.e. grid 4 and grid 5, respectively). This is done by centring the inner and intermediate grids on the density maximum of the galaxy in question. Alternatively, the centre of mass can be considered. Particles outside R_{sys} are lost, compare the discussion above. The code is not restricted to one galaxy. Since the potentials, and thus the accelerations, are additive, all galaxies are treated sequentially in the same five grids. The corresponding five total potentials are Φ_1 , Φ_2 , Φ_3 , Φ_4 , and Φ_5

- (i) For a particle with $r < R_{\text{core}}$, the correct potential is $\Phi_1 + \Phi_3 + \Phi_5$.
- (ii) For a particle with, $R_{\text{core}} < r < R_{\text{out}}$ the sum $\Phi_2 + \Phi_3 + \Phi_5$ is taken.
- (iii) When the particle is outside R_{out} then Φ_4 and Φ_5 are used.

In principle, number and type of the galaxies is arbitrary.

Two features should be emphasized. A particle at the point (x, y, z) is assigned to the cell with indices

$$a = \left[\gamma x + \frac{N}{2} \right], \quad b = \left[\gamma y + \frac{N}{2} \right], \quad c = \left[\gamma z + \frac{N}{2} \right] \quad (7)$$

where $[\]$ denotes the nearest integer function. The factor γ enhances (or shrinks) an area. If $\gamma = 10$ is assigned to grid 1, the resolution increases by a factor of 10. Inside the cell with indices i, j, k , let the particle’s coordinates be $\Delta x, \Delta y$, and Δz . Then its acceleration, e.g. in x -direction is found by the expression

$$a_x = \frac{\Phi_{i+1,j,k} - \Phi_{i-1,j,k}}{2l_x} + \frac{\Phi_{i+1,j,k} + \Phi_{i-1,j,k} - 2\Phi_{i,j,k}}{l_x^2} \Delta x + \frac{\Phi_{i+1,j+1,k} - \Phi_{i-1,j+1,k} + \Phi_{i-1,j-1,k} - \Phi_{i+1,j-1,k}}{4l_x l_y} \Delta y + \frac{\Phi_{i+1,j,k+1} - \Phi_{i-1,j,k+1} + \Phi_{i-1,j,k-1} - \Phi_{i+1,j,k-1}}{4l_x l_z} \Delta z \quad (8)$$

where $l_x = l_y = l_z$ is the length of the cell. This scheme requires two empty cells at each boundary, i.e., only $N-4$ cells per dimension are considered. We note that in SUPERBOX, the three lengths are equal. When all velocities are updated by applying these accelerations, then new positions of the particles are calculated. After that, a new integration cycle starts.

2.2 Extensions to SUPERBOX-10

For version 10, SUPERBOX’s original FORTRAN 77 code has been ported to FORTRAN 95 and arranged into several modules, to make future extension easier.

2.2.1 Individual masses

The conventional particle-mesh technique considers only a single mass for all particles. In SUPERBOX-10, an individual mass can be assigned to each particle. In practice, however, the particles of each subgroup (i.e. halo, disc, etc.) carry identical mass.

2.2.2 Improved vertical resolution

SUPERBOX poorly resolves stellar discs in vertical direction. SUPERBOX-10 overcomes this shortcoming. We explain the basic idea by taking the example of a disc-bulge-halo galaxy. First, the potential of the disc-bulge-halo galaxy is calculated. The intermediate grids grid 2 and grid 3 are flattened along the corresponding z -axis. When, for instance, the flattening is $q = 1/4$ the resolution is improved by a factor of 4. As a consequence, equations 2, 7 and 8 need to be changed. Yet, there is a restriction to q . In order to cover grid 1 and at least two cells of grid 4 (and 5, respectively), q should not be smaller than

$$q_{\text{crit}} = \max \left(\frac{R_{\text{core}}}{R_{\text{out}}}, \frac{4}{N-4} \frac{R_{\text{sys}}}{R_{\text{out}}} \right) \quad (9)$$

Otherwise, spurious results are obtained. If more than one galaxy is considered, $q < 1$ applies only to the first galaxy.

Bien et al. (2008) simulated a disc-bulge halo galaxy using SUPERBOX-10. The authors made a comparison with a code based on the TREE-GRAPE scheme (Fukushige, Makino & Kawai 2005). For 2,577,235 particles the CPU time turned out to be about three days on a single

Table 1. Maximum and achieved speed-up, S_{\max} and S , as function of grid size N and particle number n . $f = t_{\text{FFT}}/t_{\text{tot}}$, see text.

| N | n | f | S_{\max} | S | S/S_{\max} |
|-----|------|------|------------|-------|--------------|
| 64 | 500k | 0.62 | 2.61 | 2.48 | 0.95 |
| 128 | 500k | 0.92 | 12.58 | 8.96 | 0.71 |
| | 2M | 0.74 | 3.80 | 3.26 | 0.86 |
| 256 | 500k | 0.99 | 71.56 | 23.49 | 0.33 |
| | 2M | 0.95 | 20.20 | 11.90 | 0.59 |
| | 10M | 0.78 | 4.48 | 4.05 | 0.90 |

GRAPE6a board. The CPU time of SUPERBOX-10 (which is still called SUPERBOX in that paper) on a customary PC is of the same order. This result shows impressively the efficiency of the code. Bien et al. (2008) came to the conclusion that the extended code

- (i) is very fast,
- (ii) does not produce noticeable numerical disc heating, and
- (iii) allows an improved vertical resolution.

2.2.3 Parallelisation

The computationally most intensive part of SUPERBOX-10 is the calculation of the potential using the Fast Fourier Transform. The non-parallelised version of SUPERBOX-10 applies the 1D-FFT routine REALFT, taken from *Numerical Recipes* (Press et al. 1992). The 3D-FFT is calculated by doing $N \times N$ 1D transforms in each direction. In the parallelised version, this scheme has been replaced by a 3D-FFT from the FFTW library (version 2.1.5), see Frigo & Johnson (2005). This routine divides the 3D array into slices along one dimension and distributes these slices among multiple processors. The processors then jointly calculate the 3D-FFT, using the Message Passing Interface to communicate. The modular design of SUPERBOX-10 allows us to replace the FFT routine without changing much of the rest of the code. The non-parallelised FFT is still available.

In the following we introduce the fraction $f = t_{\text{FFT}}/t_{\text{tot}}$ in order to analyse the non-parallelised version in more detail. Here t_{FFT} is the time spend in the FFT routine per integration step and t_{tot} is the total time used for the integration step. According to Amdahl’s law (Amdahl 1967), the maximum achievable speed-up by improving the FFT is then given by

$$S_{\max} = \frac{1}{1-f} \quad (10)$$

Table 1 lists f , S_{\max} and the speed-up S achieved in benchmarks.

The values depend on the grid size N as well as on the particle number n . For $n \gtrsim N^3$, the integration of the particles’ orbits starts to dominate over the potential calculation. Thus, the higher N , the greater the expected speed-up will be.

Benchmarks were run on the Titan cluster at the Astronomisches Rechen-Institut, which has 32 nodes, each containing a Xeon 3.2 Ghz dual core CPU and a nVidia GeForce 9800 GTX Graphics Processing Unit (GPU). However, we

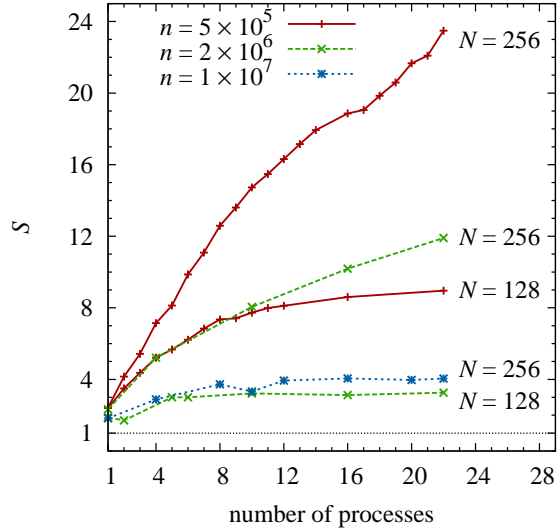


Figure 3. Speed-up S compared to non-parallelised SUPERBOX as function of the number of processors for varying N^3 , the number of grid cells, and particle number n .

used only one core per CPU in order to have more memory available, allowing for higher grid sizes. The GPUs are currently not used by SUPERBOX-10, but a version suitable for GPUs is in preparation.

Figure 3 shows the measured speed-up S as function of the number of processes in comparison to the non-parallelised version of SUPERBOX with the old FFT when varying both the grid cell number N and the particle number n . The application of FFTW alone already results in a speed-up between 1.8 and 2.4. In cases where the curves reach their maximum ($N = 256$ for $n = 10 \times 10^6$ and $N = 128$ for all n) the speed-up lies between 0.7 and 0.9 S_{\max} . In the remaining two cases ($N = 256$ for $n = 0.5 \times 10^6$ and $n = 2 \times 10^6$) it lies between 0.3 and 0.6 S_{\max} . When more processors are applied one can expect a further increase.

The fact that the speed-up almost reaches S_{\max} shows that there is only a small overhead due to communication between the nodes. Thus, from the values of S_{\max} in Table 1 we can formulate the following rule of thumb: When using p processors and a grid of size N^3 , the number of particles should not be greater than $4N^3/p$. Conversely, when simulating n particles with a grid of size N^3 , no more than $4N^3/n$ processors should be used.

3 MODELS

In this section we will describe the models used in our simulations of isolated disc-bulge-halo galaxies (section 4) and merging of galaxies with satellites (section 5).

3.1 Galaxy model

Our galaxy model consists of a disc, a bulge and a dark matter halo component. The density profile of the disc is exponential in radial and isothermal in vertical direction for $R < R_{\max}$ and $|z| < z_{\max}$:

Table 2. The three components of our galaxy model and the satellite. Shown are the number of particles n , the total mass M and the mass per particle m .

| | n [10^6] | M [$10^{10} M_\odot$] | m [$10^3 M_\odot$] |
|-----------|----------------|---------------------------|------------------------|
| disc | 5.19 | 4.82 | 9.30 |
| bulge | 2.30 | 2.14 | 9.30 |
| halo | 2.15 | 20.0 | 93.0 |
| satellite | 0.50 | 0.54 | 10.08 |

$$\varrho(R, z) = \varrho_0 e^{-R/h} \operatorname{sech}^2(z/z_0) \quad (11)$$

The disc has a scale length $h = 2.5$ kpc and a thickness $z_0 = 0.6$ kpc. The profile is cut off at $R_{\max} = 10 h$ and $z_{\max} = 10 z_0$. This excludes 0.05 per cent of the mass an infinite profile would have. At $R = 8$ kpc the Toomre parameter has a value of $Q = 2$.

Both bulge and halo have a cropped Hernquist profile (Hernquist 1990)

$$\varrho(r) = \varrho_0 \frac{a^4}{r(r+a)^3} \quad (12)$$

with scale radius a and cutoff radius r_c .

The scale radius of the bulge is $a = 0.5$ kpc and is cut off at $r_c = 14 a$. The halo's scale radius is $a = 16.8$ kpc and it is cut off at $r_c = 5 a$.

We emphasize that both bulge and halo are represented by live particles. The importance of treating the dark matter halo of galaxies as a live component, i.e., dynamically evolving and in mutual interaction with the baryonic component, has been stressed in self-consistent N -body simulations of isolated disc galaxies (e.g., Athanassoula 2002; Dubinski, Berentzen & Shlosman 2009). The angular momentum exchange between the disc and dark matter halo in such cases is mediated by dynamical resonances. These processes cannot be resolved when using a static, e.g., analytic prescription for the halo potential.

The model has been implemented with the programme MAGALIE (Boily, Kroupa & Peñarrubia-Garrido 2001). We extended MAGALIE to allow for up to 10 million particles.

The particle numbers and masses of the three components are listed in Table 2. In order to reduce the total number of particles, the particles of the halo are chosen to be ten times as massive as those of disc and bulge. This does not pose a problem though, because they are still light enough not to cause numerical heating.

Initially, the model is not completely in equilibrium. Therefore, it is evolved in isolation with high resolution ($N = 256$, $q = 0.25$) until it reaches equilibrium. This resolution is high enough not to introduce any numerical heating.

Figure 4 shows the disc's mean rotational velocity $\langle v_\Phi \rangle$ and its velocity dispersions σ_R and σ_z in radial and vertical direction after this initial relaxation. Also shown is the circular velocity v_c . The stellar disc has a flat rotation curve and an exponentially decreasing velocity dispersion.

3.2 Satellite model

The satellite for the merger simulations has a Plummer profile

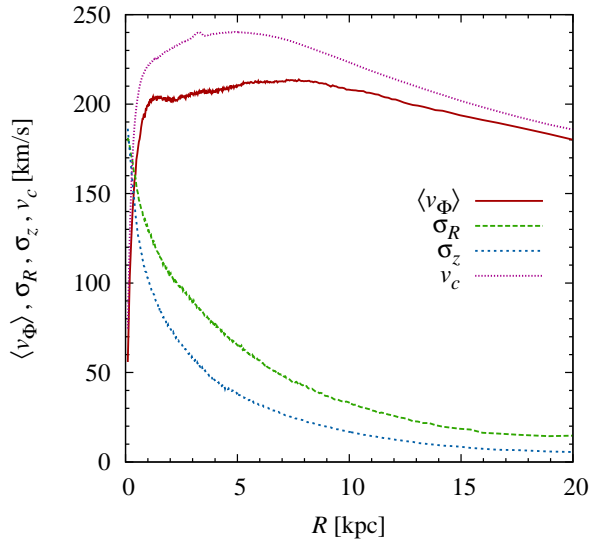


Figure 4. The disc's mean rotational velocity $\langle v_\Phi \rangle$, radial velocity dispersion σ_R , and vertical velocity dispersion σ_z . Also shown is the circular velocity v_c . Note that the galaxy has already reached equilibrium.

Table 3. Vertical resolution in parsec for various combinations of q and N . Note that $R_{\text{out}} = 28$ kpc. The radial resolution is independent of q and has the same value as the vertical resolution for $q = 1$.

| $q \setminus N$ | 64 | 128 | 256 | 512 |
|-----------------|-----|-----|-----|-----|
| 1 | 933 | 452 | 222 | 110 |
| 1/2 | 467 | 226 | 111 | 55 |
| 1/4 | 233 | 113 | 56 | 28 |
| 1/8 | - | 56 | 27 | 14 |

$$\rho(r) = \frac{3M}{4\pi a^3} \left(1 + \frac{r^2}{a^2}\right)^{-\frac{5}{2}} \quad (13)$$

with mass $M = 5.4 \times 10^9 M_\odot = 0.11 \times M_{\text{disc}}$ and scale radius $a = 1.5$ kpc. Its profile is cut off at $r_c = 10 a$. It consists of 5×10^5 particles (see Table 2). Like the galaxy, it is first evolved in isolation.

4 ISOLATED GALAXY MODELS

Bien et al. (2008) showed that SUPERBOX intrinsically has a very low level of numerical heating. We discuss now in detail the dependence of the numerical heating on the vertical flattening factor q . To that end we simulate the previously discussed disc-bulge-halo galaxy model in isolation with various resolutions and measure the change in vertical thickness of the disc component.

4.1 Simulation parameters

In all simulations, the grids have $R_{\text{core}} = 3.5$ kpc, $R_{\text{out}} = 28$ kpc and $R_{\text{sys}} = 105$ kpc. Depending on the number of cells N^3 and flattening parameter q , the simulations have vertical resolutions listed in Table 3. The radial resolution

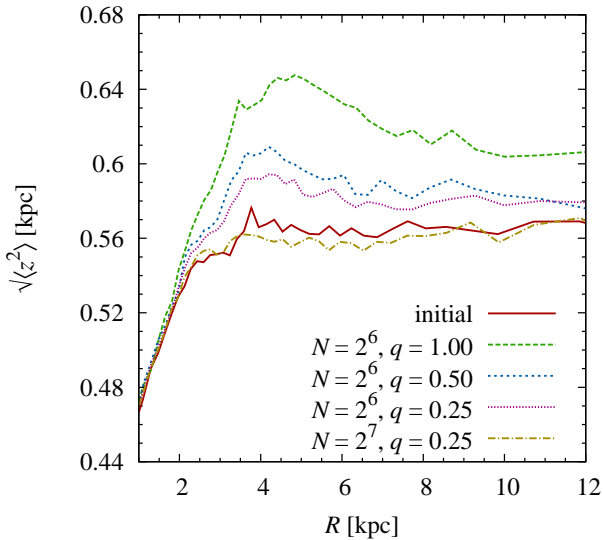


Figure 5. Standard deviation of the z -coordinate of disc particles as function of R for varying N and q at $t = 1$ Gyr, together with the initial curve. The values are calculated in radial bins of equal particle numbers.

for a certain $N = N_0$ has the same value as the vertical resolution for $N = N_0$ and $q = 1$.

We run low-resolution simulations with $N = 64$ and $q = 1, 0.5, 0.25$. The radial resolution is 933 pc and the vertical resolution amounts to 933, 467 and 233 pc, respectively. These simulations are compared to a medium-resolution simulation ($N = 128, q = 0.25$) where the radial resolution is 452 pc and the vertical resolution is 113 pc. Additionally, a comparison to the initial, relaxed, system is made. A time step of 0.4 Myr is used and the length of the integration corresponds to 1 Gyr.

4.2 Results

Figure 5 shows the root mean square (RMS) of the z -coordinate of all disc particles, $\sqrt{\langle z^2 \rangle}$, as a function of radial distance R . We used radial bins of equal particle numbers. The RMS can be taken as a measure of the thickness of the disc. The low-resolution simulation ($N = 64, q = 1$) overestimates the thickness significantly. The maximum deviation from the initial thickness is about 16 per cent. Flattening the intermediate grid by a factor of 4, brings the thickness down to within about 4 per cent of the initial values, without increasing the computation time. The medium-resolution simulation ($N = 128, q = 0.25$) deviates at most ≈ 1.6 per cent from the initial values, but is closer than 1 per cent for most of the radial range.

To demonstrate the effect of flattening, Figure 6 directly compares two simulations with the same vertical resolution – $N = 128$ with $q = 0.25$ and $N = 256$ with $q = 0.25$ – corresponding to a vertical cell length of about 112 pc. As a reference the case of $N = 128$ without flattening is also shown. As can be seen, introducing flattening in the case of medium resolution diminishes thickness, down to about the same value as in the case of high resolution.

Figure 7 displays the vertical density profile averaged

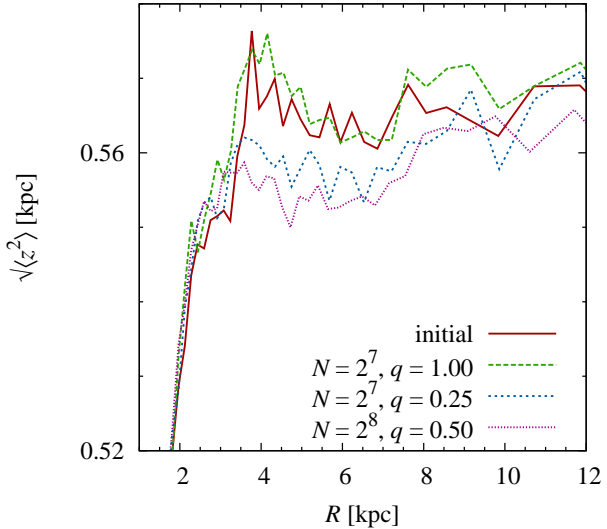


Figure 6. Standard deviation of the z -coordinate of disc particles as function of R for varying N and q at $t = 1$ Gyr, together with the initial curve. The values are calculated in radial bins of equal particle numbers.

over the radial interval $7.5 \text{ kpc} \leq R \leq 8.5 \text{ kpc}$. The initial profile (solid line) and the profile of the medium-resolution simulation (dash-dotted line) are almost identical. In the case of the low-resolution simulations (dashed line), the profile is significantly widened for $|z| > 1 \text{ kpc}$ (see Figure 7 (b)). This is a sign of numerical heating. Reducing q brings the profile closer to the initial one. For $q = 0.25$, deviations are only visible beyond 2 kpc.

Figure 8 shows the time evolution of the RMS for varying grid size N and flattening factor q in the region around $R = 8 \text{ kpc}$. In the first 200 Myr, the model adapts to the new grid structure, which causes a change in the RMS. After that, the RMS increases slightly with time in the case of the low-resolution simulations. It reaches values that are 8.7 per cent ($q = 1$), 3.6 per cent ($q = 0.5$) and 2.4 per cent ($q = 0.25$) greater than the initial value. In the medium-resolution simulation however, it remains stable at a deviation of about 0.9 per cent.

5 MERGER SIMULATIONS

One application that benefits from the increased z -resolution is the study of the dynamical heating of galactic discs caused by the merging with satellite galaxies. We simulate the merging of a small satellite with a disc-bulge-halo galaxy for varying initial positions and velocities of the satellite.

5.1 Simulation parameters

All satellites are initially at a distance of $R_A = 25 \text{ kpc}$ from the centre of the galaxy and have a velocity of either 115 km s^{-1} or 81.3 km s^{-1} . If all the mass of the galaxy inside R_A were concentrated in a point mass, these velocities would result in elliptical orbits with apocentre distance R_A and eccentricities $\epsilon = 0.56$ and $\epsilon = 0.78$, respectively. Here, the eccentricity is defined as

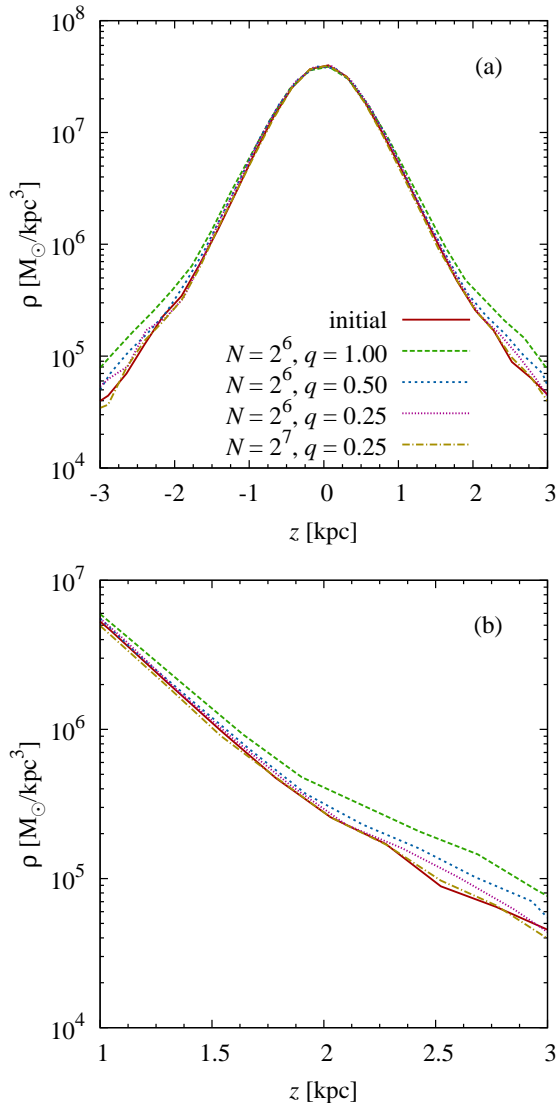


Figure 7. Volume density ρ as function of z (averaged over the radial range $7.5 \text{ kpc} \leq R \leq 8.5 \text{ kpc}$) for varying N and q at $t = 1 \text{ Gyr}$. The solid line shows the initial values. (a) Whole range. (b) Right tail.

Table 4. Satellite parameters ϵ (eccentricity), v (velocity), R_A (apocentre), R_P (pericentre) and i (orbital inclination).

| ϵ | v [km/s] | R_A [kpc] | R_P [kpc] | i [°] |
|------------|------------|-------------|-------------|-----------------|
| 0.56 | 115 | 25 | 7.05 | 0, 10, ..., 180 |
| 0.78 | 81.3 | 25 | 3.08 | 0, 10, ..., 120 |

$$\epsilon = \frac{\sqrt{a^2 - b^2}}{a}$$

with semi-major axis a and semi-minor axis b . In the two-body problem, the pericentre distance of these orbits would be $R_P \approx 7 \text{ kpc}$ and $R_P \approx 3 \text{ kpc}$, respectively.

In addition to the eccentricity, we vary the orbital inclination i relative to the plane of the disc between 0° and 180° for $\epsilon = 0.56$ in steps of 10° , and likewise between 0° and 120° for $\epsilon = 0.78$. For $i < 90^\circ$ the satellite is on a pro-

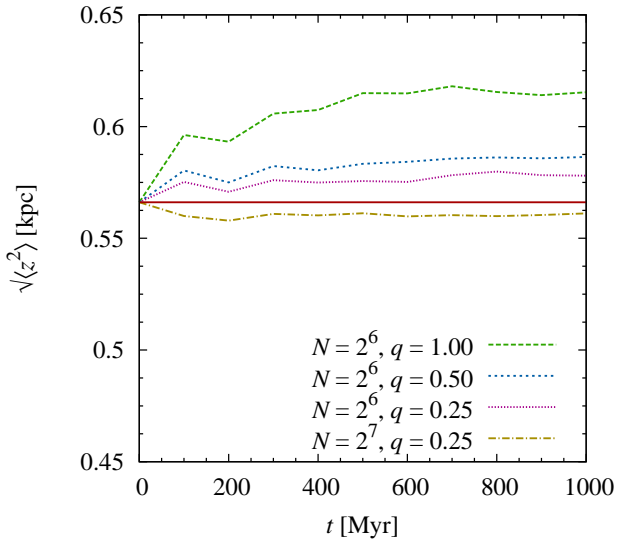


Figure 8. Standard deviation of the z -coordinate of disc particles as function of time for varying grid size N and flattening q . The standard deviation is calculated in a region around $R = 8 \text{ kpc}$. The solid line shows the initial value.

grade orbit as compared to the galactic rotation, while for $i > 90^\circ$ the orbit is retrograde. For $i = 90^\circ$ the satellite's initial velocity is perpendicular to the bulk motion of the disc. Table 4 summarises these parameters.

As shown in the previous section, a grid cell number of $N = 128$ with flattening factor $q = 0.25$ causes no significant numerical heating. We adopt these values for our merger simulations. All simulations run for 1 Gyr. After that, the satellites are completely dissolved. As a control, the galaxy model is also evolved in isolation.

At the end of the simulation, the plane of the disc is tilted by a few degrees. In the following, the data are evaluated in a coordinate system where x and y define the galactic plane and z is perpendicular to it.

5.2 Vertical profile

Figure 9 shows the vertical density profile of the disc after merging. Only satellites with significant effect on the disc are shown ($e = 0.56$, $i = 0^\circ \dots 30^\circ$). Compared to the isolated simulation (i.e. without satellite), the central density is decreased by a factor of 2 at the most ($i = 20^\circ$). In the inner part ($|z| < 1 \text{ kpc}$), the original $\text{sech}^2(z/z_0)$ profile remains a good fit, albeit with a greater thickness z_0 . The isolated galaxy has $z_0 = 0.6 \text{ kpc}$, while for $i = 20^\circ$ the thickness is increased to 0.8 kpc . In the outer part, however, the density is increased as compared to a $\text{sech}^2(z/z_0)$ law. While the thickness of 0.8 kpc corresponds to a scale height of 0.4 kpc , the outer part is better fitted by an exponential function with scale height $\approx 0.65 \text{ kpc}$.

Hayashi & Chiba (2006) provide a formula for the increase of the thickness of the disc caused by cold dark matter subhaloes, which should also be applicable to satellite mergers. In our notation their formula is given by

$$\Delta z_0 \approx 8h \left(\frac{M_{\text{sat}}}{M_{\text{disc}}} \right)^2 \approx 0.25 \text{ kpc}.$$

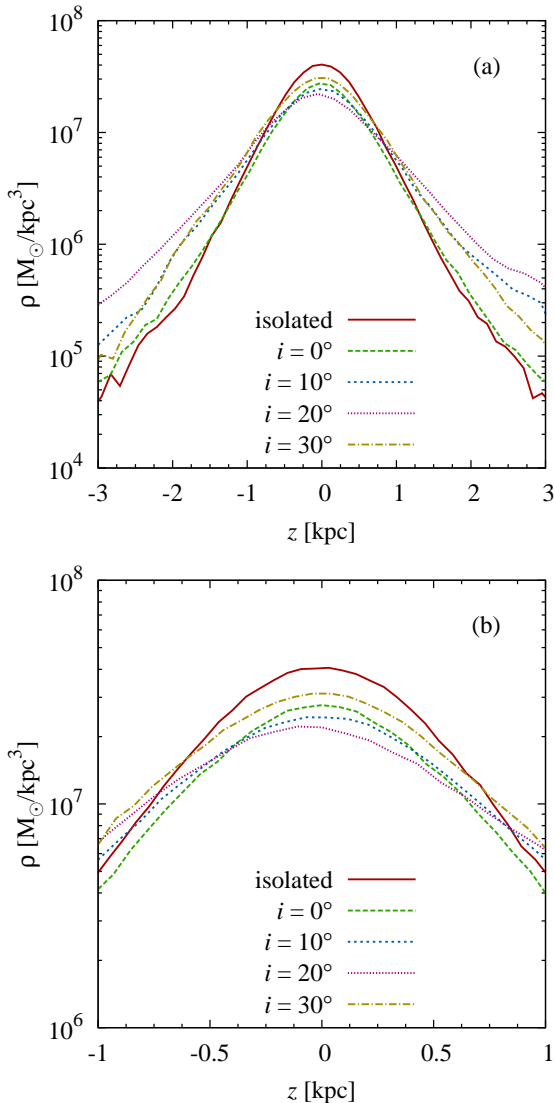


Figure 9. Volume density of the disc in the region $7.5 \text{ kpc} \leq R \leq 8.5 \text{ kpc}$ after the merging ($t = 1 \text{ Gyr}$) as function of z for different satellite orbital inclinations i . All satellites show have initial orbital eccentricity $\epsilon = 0.56$. The solid line corresponds to the isolated simulation, i.e., without satellite. (a) Whole range. (b) Inner part.

This is compatible with an increase of $\Delta z_0 \gtrsim 0.2 \text{ kpc}$ in the case of $i = 20^\circ$ as described above.

5.3 Heat increase

We define the total heat in the disc as the kinetic energy of random motion

$$E_{\text{heat}} = \sum_i \frac{1}{2} m_i |\mathbf{v}_i - \bar{\mathbf{v}}_c(R_i)|^2 \quad (14)$$

where the sum goes over all particles in the disc, m_i is the mass of the i th particle, \mathbf{v}_i is the velocity of the i th particle, and $\bar{\mathbf{v}}_c(R_i)$ is the mean circular velocity at the radial distance R_i of the i th particle. \mathbf{v}_c is first calculated in radial bins of equal particle numbers and then interpolated to the individual distances R_i .

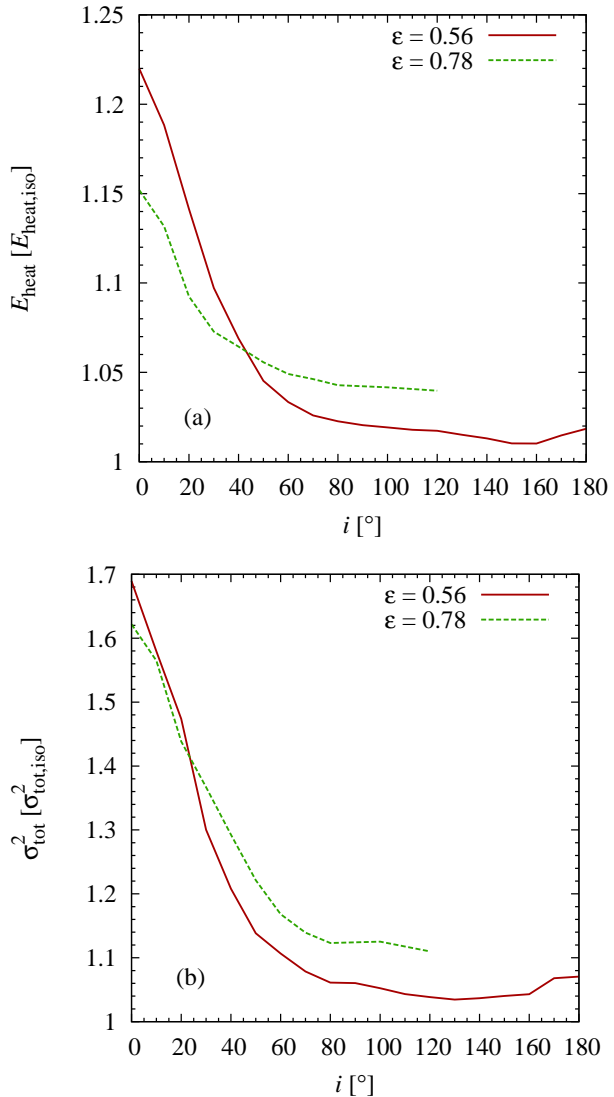


Figure 10. (a) Total heat of the disc after merging ($t = 1 \text{ Gyr}$) as a function of satellite's orbital inclination i for varying eccentricity ϵ . E_{heat} is measured in units of the heat of the isolated galaxy, $E_{\text{heat,iso}}$, at $t = 1 \text{ Gyr}$. (b) Squared total velocity dispersion at $t = 1 \text{ Gyr}$ in the region around 8 kpc as a function of orbital inclination i and for varying eccentricity ϵ . σ_{tot}^2 is measured in units of the squared total velocity dispersion of the isolated galaxy.

Figure 10 (a) shows E_{heat} in units of the heat in the isolated disc $E_{\text{heat,iso}}$ at the end of the simulation (i.e. at $t = 1 \text{ Gyr}$). $E_{\text{heat,iso}}$ increases only by 0.18 per cent as compared to the initial value, demonstrating that our simulations are free of numerical heating. Figure 10 (b) displays the same for the square of the total velocity dispersion in the solar neighbourhood.

The heating efficiency of the satellite depends on its orbital inclination as well as on its orbital eccentricity. For low inclinations, satellites on less elliptical orbits heat more effectively than those on more elliptical ones. For $i > 40^\circ$, however, satellites on orbits with $\epsilon = 0.78$ are more effective. Prograde satellites heat the most with an maximum increase of 22 per cent, while retrograde ones only have a small effect

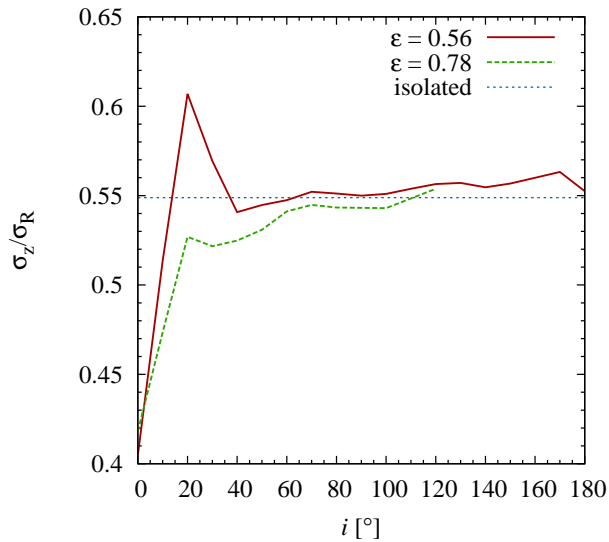


Figure 11. Velocity dispersion ratio σ_z/σ_R at $t = 1$ Gyr in the region around 8 kpc as function of orbital inclination i and for varying eccentricity ϵ .

of about 2 per cent. These results are consistent with those obtained by Velazquez & White (1999).

Observations show that the velocity dispersion in the solar neighbourhood increases from about 30 km s^{-1} to about 60 km s^{-1} in 8 Gyr approximately proportional to \sqrt{t} (see, e.g., Hänninen & Flynn 2002). This means, that the specific heat increases linearly by about $1350 \text{ km}^2 \text{ s}^{-2}$. If we assume that the heat increase is completely due to satellite mergers, then the required merger rate n is

$$\nu = \frac{1}{\Delta h} \times \frac{1350 \text{ km}^2}{8 \text{ s}^2 \text{ Gyr}} \quad (15)$$

where Δh is the specific heat increase imparted by a single merger.

In our simulations, we found that for low inclinations the heat increase is approximately uniform over the whole disc (except for the bulge-dominated inner part) and lies between 100 and $1000 \text{ km}^2 \text{ s}^{-2}$ per merger. For high inclinations, the heat increase is mainly due to flaring of the outer parts of the disc ($R > 15 \text{ kpc}$), while the solar neighbourhood is basically unaffected. Only considering low inclinations, the required merger rate then lies between $\nu = 0.17$ and $\nu = 1.69$ mergers per Gyr, depending on inclination and eccentricity of the orbit.

5.4 Velocity dispersion ratio

Observations show that the current ratio of the radial and vertical velocity dispersions in the solar neighbourhood, σ_z/σ_R , is approximately 0.5 ± 0.1 and increases slightly with stellar age, $\propto t^{0.16}$ (Holmberg et al. 2007). Figure 11 shows this ratio after merging as a function of orbital inclination i . The satellites with low prograde orbits decrease the ratio to at most about 0.4, i.e., they heat more efficiently in radial than in vertical direction. In one case ($i = 20^\circ$, $\epsilon = 0.56$) there is an increase to approximately 0.6. For inclinations above 30° the ratio remains mostly unchanged in the solar neighbourhood.

5.5 Energy and angular momentum transfer

An interesting question is where the initial energy and angular momentum of the satellite end up in the final system.

Figure 12 shows the change in energy of the various components. The energy is measured in units where the total energy of the isolated galaxy is -1 . “Satellite” designates those particles that once made up the satellite, but now are distributed over the whole system.

The initial galaxy-satellite system is not in equilibrium. As a consequence of virialisation, both the satellite and the halo gain kinetic and lose potential energy. This results in a deeper potential well in the centre, which reduces the potential energy of bulge and disc. During its in-spiral, the satellite transfers part of its kinetic energy to the halo particles. This is due to dynamical friction.

This effect can also be seen in Figure 13, which shows the change in angular momentum as a function of inclination, measured in units of the total angular momentum of the isolated galaxy. The angular momentum of the bulge barely changes. This is not surprising since the satellites are already mostly destroyed before reaching the inner part of the galaxy. Our data reveal that the radial distribution of angular momentum in the disc changes: the disc slows down and expands. Its *total* angular momentum, however, remains approximately nearly constant. It only increases slightly for satellites on prograde orbits and decreases slightly for satellites on retrograde orbits. The satellite’s initial orbital angular momentum is 0.31 in these units. Accordingly, it loses between 15 per cent and 20 per cent of its angular momentum. Of that, about 80 per cent goes into the halo, while the rest is imparted onto the disc.

5.6 Comparison with higher resolution

To ensure that the choice of resolution does not influence the results we simulate a case with $\epsilon = 0.56$ and $i = 0^\circ$, and higher resolution. We choose $N = 256$ and $q = 0.125$, as this is the highest possible resolution one can achieve on our present hardware.

We calculate the Fourier transform of the density distribution of the disc at the end of the simulation in order to find possible perturbations caused by low resolution. The m th complex Fourier coefficient is given by

$$\tilde{A}_m(R_i) = \frac{1}{S_i} \sum_j M_j e^{-im\varphi_j}$$

where R_i and S_i are the central radius and area of the i th bin, the index j runs over all particles in bin i , and M_j and φ_j are the mass and polar angle of the j th particle. The amplitude of \tilde{A}_m is denoted by A_m and the phase by θ_m .

Figure 14 shows the amplitudes of the first and second mode normalised by the mean density, while Figure 15 displays the phase of the first mode. The two resolutions result in a roughly similar distribution in Fourier space. There are no strong perturbations in amplitude caused by the lower resolution. Neither is the pattern speed affected significantly.

6 CONCLUSIONS

SUPERBOX is a particle-mesh code where additional grids

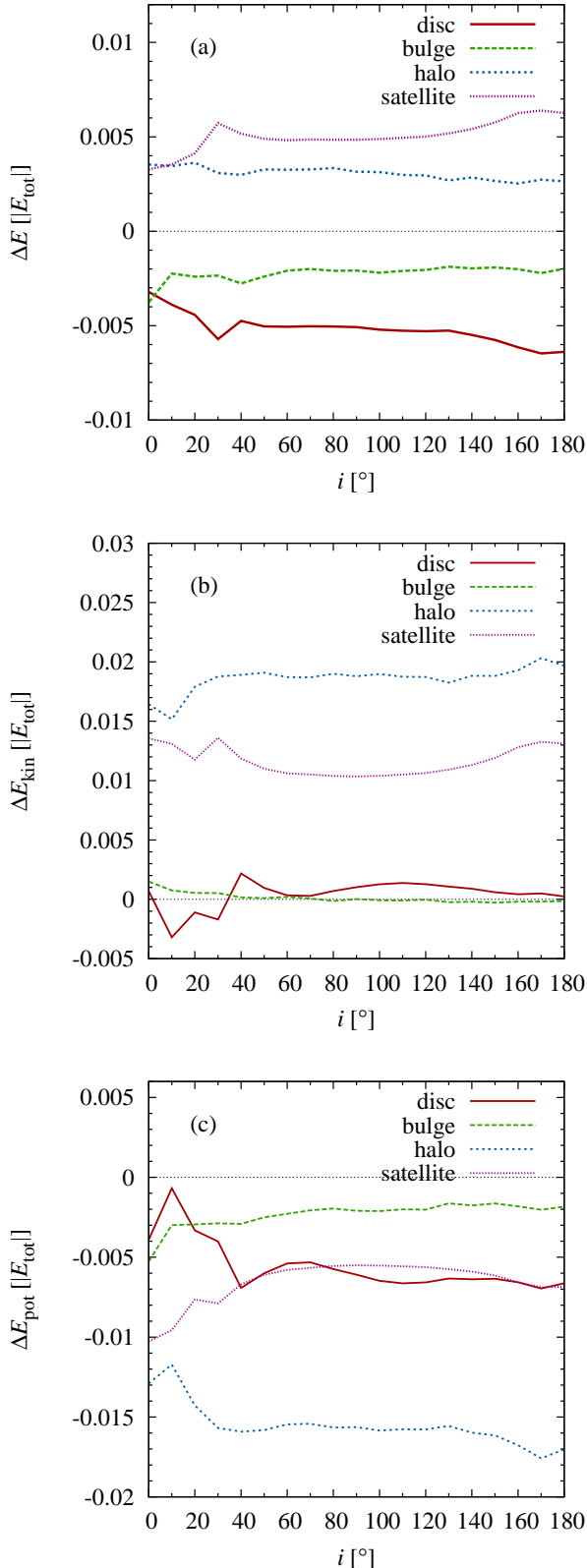


Figure 12. Change in total (a), kinetic (b) and potential (c) energy of the four components with respect to the initial energies as a function of orbital inclination i . The energy change is measured in units of the total energy of the isolated galaxy. Only the data for $\epsilon = 0.56$ is shown.

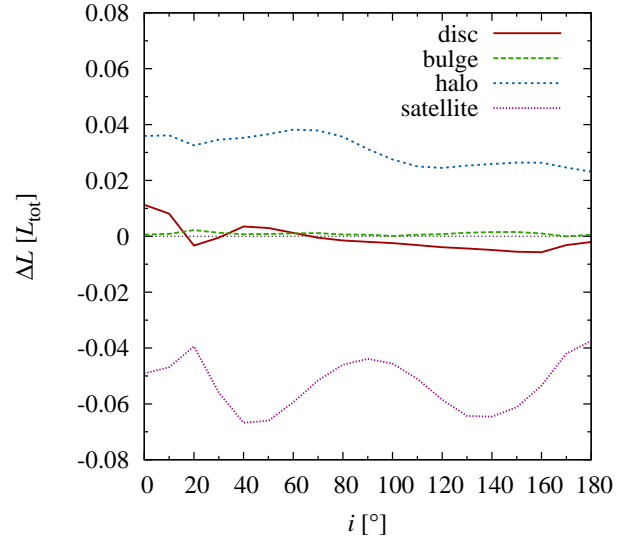


Figure 13. Change in total angular momentum of the four components with respect to the initial angular momenta as a function of orbital inclination i . The change is measured in units of the total angular momentum of the isolated galaxy. Only the data for $\epsilon = 0.56$ is shown.

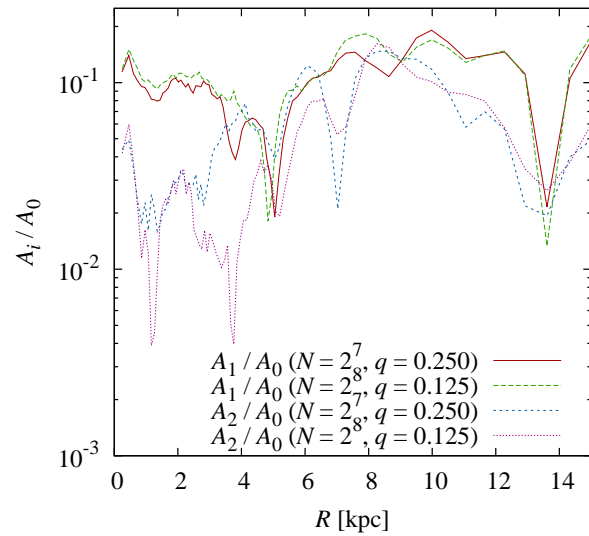


Figure 14. Amplitudes of the first and second spiral mode as a function of radius at the end of the simulation.

and sub-grids are applied to regions of high particle density. This strategy turns out to be very efficient since the code can run on any workstation or PC. Nevertheless, the code has its limitations. For instance, stellar discs are poorly resolved in vertical direction. We overcome this problem by introducing flattened grids. This is one of the features of the new code SUPERBOX-10 where, in addition, an individual mass can be assigned to each particles.

We found that the computationally most intensive part of the code is the FFT. We parallelised it using the library FFTW. This resulted in a speed-up of 2 to 24, depending on grid size N and the number of particles n .

We created a galaxy model with an exponential disc, a

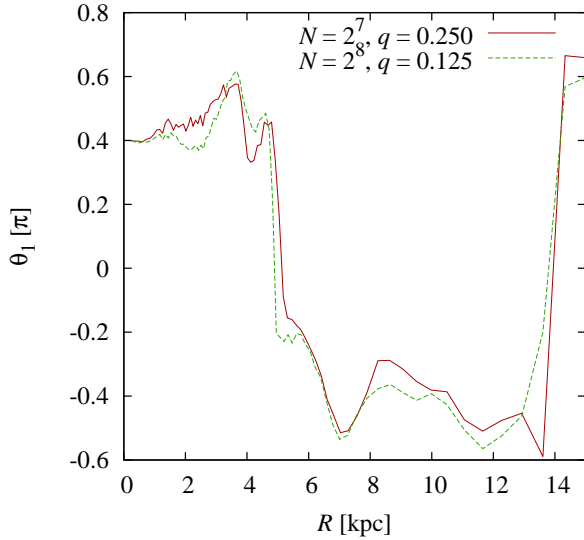


Figure 15. Phase of the first mode as a function of radius at the end of the simulation.

bulge with a Hernquist profile and a dark matter halo, also with a Hernquist profile. The model was realised using the program MAGALIE.

The model was first simulated in isolation. These simulations show that flattening the intermediate grid is an efficient means to reduce numerical heating in the simulation.

We also simulated the merging of the galaxy with small satellites in order to analyse the proposed disc heating due to the interaction. We find that satellites on prograde orbits with low eccentricity and inclination heat the disc most efficiently. If the heat increase in the solar neighbourhood were to be explained by that type of satellite mergers alone, a rate between 0.2 and 1.7 mergers per Gyr would be required. The detailed analysis of energy and angular momentum redistribution shows that most of the satellites energy and angular momentum is transferred to the dark matter halo. This shows that the halo plays an important role even in 50:1 mergers. This confirms, that simulations of such processes should represent the halo by live particles and not by a fixed background potential. The presented pilot study of high-resolution simulations of disc heating by merging satellite galaxies serves as a starting point for an extended parameter study to quantify the heating rate in a cosmological context.

ACKNOWLEDGMENTS

We thank Markus Hartmann und Ingo Berentzen for numerous and fruitful discussions.

This work was supported by Sonderforschungsbereich SFB 881 “The Milky Way System” (subproject A1) of the German Research Foundation (DFG).

The computer hardware used for the simulations was supported by project “GRACE” I/80 041-043 of the Volkswagen Foundation and by the Ministry of Science, Research and the Arts of Baden-Württemberg.

REFERENCES

- Amdahl G.M., 1967, AFIPS Conference Proceedings, 483
Ardi E., Tsuchiya T., Burkert A., 2003, ApJ, 596, 204
Athanasoula E., 2002, ApJ, 569, L83
Bien R., Fuchs B., Wielen R., 1990, in Tenner A., ed, The CP90 Europhysics Conference on Computational Physics, Singapore, p. 3
Bien R., Just A., Berczik P., Berentzen I., 2008, AN, 329, 1029
Boily C.M., Kroupa P., Peñarrubia-Garrido J., 2001, NewA, 6, 27
Carlberg R.G., 1987, ApJ, 322, 59
Carlberg R.G., Sellwood J.A., 1985, ApJ, 292, 79
Dubinski J., Berentzen I., Shlosman I., 2009, ApJ, 697, 293
Eastwood J. W., Brownrigg D. R. K., 1979, JCoPh, 32, 24
Fellhauer M., 2008, Particle-Mesh Technique and SUPERBOX in Aarseth S.J., Tout C.A., Mardling R.A., eds, The Cambridge *N*-Body Lectures, Springer-Verlag, Berlin, Heidelberg
Fellhauer M., Kroupa P., Baumgardt H., Bien R., Boily C.M., Spurzem R., Wassmer N., 2000, NewA, 5, 305
Fellhauer M., Wilkinson M.I., Evans N.W., Belokurov V., Irwin M.J., Gilmore G., Zucker D. B., Kley J. T., 2008, MNRAS, 385, 1095
Frigo M., Johnson S. G., 2005, Proceedings of the IEEE, 93, 216
Fukushige, T., Makino, J., Kawai, A., 2005, PASJ 57, 1009
Hänninen J., Flynn C., MNRAS, 337, 731
Hayashi H., Chiba M., 2006, Publ. Astron. Soc. Japan, 58, 835
Hernquist L., 1990, ApJ, 356, 359
Hockney R.W., Eastwood J.W., 1988, Computer simulation using particles, Adam Hilger, Bristol
Holmberg J., Nordström B., Andersen J., 2007, A&A, 475, 519
Hopkins P. F., Hernquist L., Cox T. J., Younger J. D., Besla G., 2008, ApJ, 688, 757
Just A., Peñarrubia J., 2005, A&A, 431, 861
Just A., Khan F.M., Berczik P., Ernst A., Spurzem R., 2010, MNRAS, 411, 653
Kazantzidis S., Bullock J. S., Zentner A. R., Kravtsov A. V., Moustakas L. A., 2008, ApJ, 688, 757
Kazantzidis S., Zentner A. R., Kravtsov A. V., Bullock J. S., Debattista V. P., 2009, ApJ, 700, 1896
Khoperskov A. V., Just A., Korchagin V.I., Jalali M.A., 2007, A&A, 473, 31
Klessen R., Kroupa P., 1998, ApJ, 498, 143
Lacey C.G., 1984, MNRAS, 208, 687
Lacey C.G., Ostriker J. P., 1985, ApJ, 299, 633
Madejsky R., Bien R., 1993, A&A, 280, 383
Naab T., Jesseit B., Burkert A., 2006, MNRAS, 372, 839
Newberg H. J., Yanny B., Rockosi C., Grebel E. K., Rix H.-W., Brinkmann J., Csabai I., Hennessy G., Hindsley R. B., Ibata R., Ivezić Z., Lamb D., Nash E. T., Odenkirchen M., Rave H. A., Schneider D. P., Smith J. A., Stolte A., York D. G., 2002, ApJ, 569, 245
Peñarrubia J., Kroupa P., Boily C.M., 2002, MNRAS, 333, 779
Peñarrubia J., Just A., Kroupa P., 2004, 349, 747
Peñarrubia J., Navarro J.F., McConnachie A.W., 2008, ApJ, 673, 226

- Press W.H., Teukolsky S.A., Vetterling W.T., Flannery B.P., 1992, *Numerical recipes in FORTRAN. The art of scientific computing*, Cambridge University Press, Cambridge
- Purcell C. W., Bullock J. S., Kazantzidis S., 2010, *MNRAS*, 404, 1711
- Quinn P.J., Hernquist L., Fullagar D.-P., 1993, *AJ*, 403, 74
- Rix H.-W., Lake. G., 1993, *ApJL*, 417, L1
- Roškar R., Debattista V.P., Stinson G.S., Quinn T.R., Kaufmann T., Wadsley J., 2008, *ApJ*, 675, L65
- Schönrich R., Binney J., 2009, *MNRAS*, 399, 1145
- Sellwood J.A., Binney J., 2001, *MNRAS*, 336, 785
- Spinnato P.F., Fellhauer M., Portegies Zwart S.F., 2003, *MNRAS*, 344, 22
- Velazquez H., White S.D.M., 1999, *MNRAS*, 304, 254
- Villalobos Á., Helmi A., 2008, *MNRAS*, 391, 1806
- Villalobos Á., Helmi A., 2009, *MNRAS*, 399, 166
- Wielen R., 1977, *A&A*, 60, 263
- Wielen R., Fuchs B., 1990, in Wielen R., ed, *Dynamics and Interactions of Galaxies*, Springer-Verlag, Berlin

This paper has been typeset from a \TeX / \LaTeX file prepared by the author.